Nanoscale

PAPER

View Article Online
View Journal | View Issue

Cite this: *Nanoscale*, 2025, **17**, 10644

Self-assembled colloidal glass with 100% lanthanide nanocrystal loading for high-resolution X-ray imaging†

Lingcheng Zeng,[a] Xin Quan,[a] Yiwen Wang,[a] Shulang Lin,*[b] Jiahui Xu*[a] and Yiming Wu *[a]

Solution-processable colloidal scintillators are emerging as a promising alternative to traditional bulky scintillators, addressing critical limitations in X-ray imaging technologies. Existing X-ray screens fabricated with colloidal powders in polymer matrices suffer from low spatial resolution at elevated particle concentrations due to severe optical losses induced by nanoparticle aggregation, fundamentally constraining high-resolution imaging capabilities. To resolve these challenges, we developed a novel class of bright, transparent colloidal glasses achieving 100% particle loading through self-assembly of sub-5 nm lanthanide-doped $CaMoO_4$ nanocrystals. By modulating solvent surface tension and volatility during the evaporation process, we successfully produced crack-free, densely packed transparent colloidal scintillator films. The self-assembled colloidal glass demonstrates an impressive 80% photoluminescence quantum yield and >80% transparency across the visible spectrum. Moreover, the developed screen exhibits remarkable sensitivity, detecting radiation doses as low as 186 nGy s^{-1} with an outstanding X-ray imaging resolution of 27.1-line pairs per millimeter, outperforming most conventional organic and inorganic scintillators. These findings illuminate a compelling pathway for utilizing nanomaterials to replace traditional single-crystal scintillators in high-resolution X-ray imaging, potentially revolutionizing medical imaging and radiation detection technologies.

Received 10th December 2024,
Accepted 24th March 2025

DOI: 10.1039/d4nr05213g

rsc.li/nanoscale

Introduction

High-energy ionizing radiation detection using advanced scintillation materials has emerged as a pivotal technological frontier, underpinning critical applications across security screening to sophisticated medical imaging and advanced industrial non-destructive testing.[1–7] For imaging purposes, transparent scintillator films offer significant advantages by minimizing light scattering and self-absorption, thus ensuring efficient light transmission and enhanced scintillation efficiency.[8–10] Consequently, these films enable high-resolution images with superior spatial clarity and contrast, which are essential for capturing intricate details in medical diagnostics and industrial inspections. Ceramic glass scintillators, including cerium-doped lutetium oxyorthosilicate (LSO:Ce), bismuth germanate (BGO), and yttrium aluminum garnet (YAG), demonstrate high transparency and excellent light output efficiency.[11–14] However, their production presents considerable challenges. The high-temperature sintering or crystallization processes required to achieve transparency and uniformity can escalate energy costs, restrict material selection due to thermal incompatibility, and necessitate meticulous control to prevent defects such as pores or scattering centers.[15–18]

Solution-processable colloidal scintillators represent a promising alternative to traditional scintillator materials, offering distinct advantages in radiation detection applications. Unlike conventional scintillators that demand complex, high-temperature processing and result in bulk, rigid materials, colloidal scintillators can be readily processed into thin, uniform films or coatings using straightforward solution-based techniques like spin-coating or evaporation. This approach enables scalable production with reduced energy expenditure. Moreover, the fine control over particle size, morphology and doping allows precise tuning of scintillator properties, including emission wavelength and efficiency—a capability more challenging to achieve with traditional materials. Nevertheless, direct drop-casting of nanoparticles often results in non-transparent films due to inherent challenges such as

[a]*Institute of Flexible Electronics (IFE, Future Technologies), Xiang'an Campus, Xiamen University, Xiang'an South Road, Xiamen 361102, Fujian, China. E-mail: ifeymwu@xum.edu.cn*
[b]*Optical Bioimaging Laboratory, Department of Biomedical Engineering, College of Design and Engineering, National University of Singapore, Singapore 117576*
† Electronic supplementary information (ESI) available. See DOI: https://doi.org/10.1039/d4nr05213g

particle aggregation and the formation of voids or cracks during the evaporation process. Consequently, for imaging applications, colloidal nanoparticles are typically incorporated into a polymer matrix to create nanocomposite films. A critical consideration in preparing nanocomposite films with scintillator nanoparticles is the delicate balance between film transparency and particle loading capacity. Increasing nanoparticle loading enhances scintillation efficiency but simultaneously increases light scattering, compromising transparency. Conversely, reducing particle loading maintains optical clarity but limits scintillation output by reducing the number of active detection sites. However, previous attempts have been constrained by low nanoparticle loadings (typically <20 wt%),[19–24] which were necessary to maintain film transparency for practical applications, thereby inherently limiting high-resolution imaging performance.

Herein, we present an evaporation-induced self-assembly approach for fabricating transparent colloidal glass scintillator films with 100% nanocrystal loading. Ultra-small lanthanide (Ln^{3+})-doped $CaMoO_4$ nanocrystals (NCs) were used as scintillator materials due to their high quantum yield (>80%)[25,26] and wide bandgap, which effectively suppressed self-absorption. Additionally, $CaMoO_4$:Ln^{3+} nanocrystals have been synthesized *via* room-temperature co-precipitation, a process that allows easy modification without requiring high-temperature procedures. By optimizing evaporation conditions, we successfully produced crack-free, densely packed nanocrystalline scintillator films. This was achieved by carefully balancing the evaporation process using solvents with moderate surface tension and volatility. The resulting colloidal glass film demonstrates excellent transparency over 80% across the visible wavelength range. Furthermore, $CaMoO_4$:15%Eu^{3+} glass screens exhibit an impressive X-ray imaging resolution of over 27.1 lp mm^{-1}, surpassing most recognized organic and conventional inorganic scintillators. These findings pave the way for the use of nanomaterials to replace traditional single-crystal scintillators in high-resolution X-ray imaging applications.

Yiming Wu

*Yiming Wu received his PhD in Chemistry from the National University of Singapore (NUS) in 2018 under the mentorship of Professor Xiaogang Liu. He completed a three-year postdoctoral fellowship at NUS, focusing on advanced nanomaterial synthesis. He then worked as a research scientist at the Institute of Materials Research and Engineering (IMRE), Agency for Science, Technology and Research (A*STAR), Singapore. Dr Wu is currently a Professor at the Institute of Flexible Electronics (Future Technologies), Xiamen University, China. His research interest lies in the rational design of frequency conversion nanomaterials for optoelectronic applications.*

Results and discussion

The fabrication of high-quality transparent nanocrystal films requires precise management of colloidal stability, self-assembly, and structural integrity during preparation. Three critical parameters govern film quality: first, particle size fundamentally influences film properties. Smaller nanocrystals demonstrate superior packing density and uniformity, minimizing structural voids and refractive index mismatches. Additionally, according to Rayleigh scattering principles, reduced particle dimensions substantially decrease light scattering, thereby enhancing film transparency. Second, ligand selection emerges as a pivotal factor in nanocrystal film formation. Short-chain ligands, such as butyric acid and butylamine, are particularly effective in stabilizing nanocrystals while facilitating close packing during film preparation. Complete and uniform ligand coverage prevents particle aggregation and maintains colloidal stability in solution. Third, solvent selection critically influences the evaporation process. Optimal solvents possess carefully balanced evaporation rates, providing sufficient time for nanocrystals to self-assemble into dense, defect-free structures while minimizing capillary stress and preventing cracking. Conversely, rapid or uneven evaporation can induce significant shrinkage stress, resulting in structural defects.

To address potential scattering challenges, we synthesized highly efficient $CaMoO_4$:15%Eu^{3+} nanocrystals *via* a simple, room-temperature ligand-assisted coprecipitation method (Fig. 1a). The capping effect of butyric acid and butylamine ligands during crystal formation resulted in remarkable stability (Fig. 1b). High-resolution transmission electron microscopy revealed an average nanocrystal size of 3.5 nm, with exceptional dispersion and minimal agglomeration (Fig. 1c, d and Fig. S1†).

Fig. 1e shows the schematic illustrating the self-assembly process for fabricating a colloidal scintillator glass. PDMS is renowned for its ability to inhibit random cracking in photonic crystals and particle coatings, attributed to its low surface energy and hydrophobic properties.[27–29] By dispersing $CaMoO_4$:15%Eu^{3+} NCs in hexanol and casting the solution into a Petri dish coated with a layer of polydimethylsiloxane (PDMS) substrate, transparent colloidal film was obtained after solvent evaporation at room temperature. This process yielded a 250 μm thick colloidal glass film with a remarkably intact structure devoid of cracks atop the PDMS (Fig. 1g and k). In contrast, colloidal dispersions in cyclohexane produced only a white opaque solid (Fig. 1f and j). $CaMoO_4$ and $CaMoO_4$:15%Eu^{3+} samples exhibited bandgap values of 3.32 eV and 3.67 eV, respectively (Fig. 1h, Fig. S2†). These wide bandgap characteristics effectively suppress unnecessary absorption in the visible light region, rendering them highly

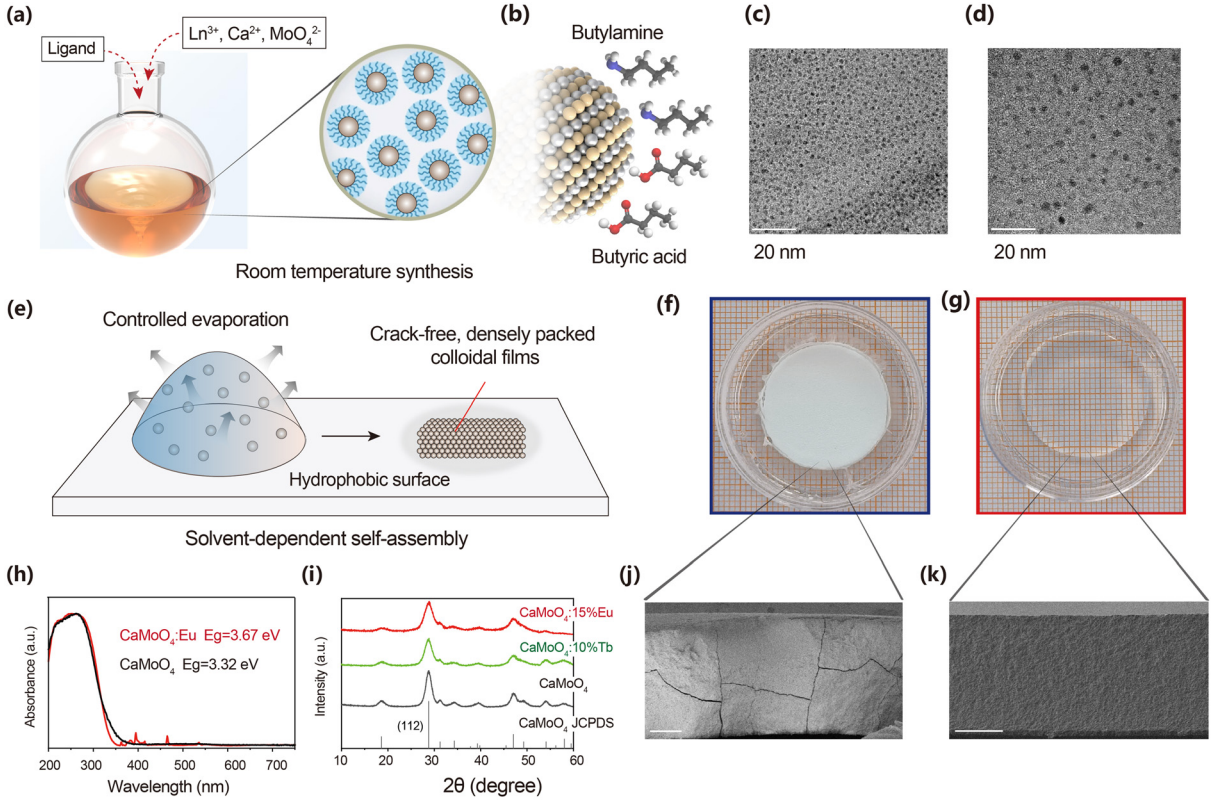

Fig. 1 Self-assembled colloidal glass scintillators. (a) Schematic illustrating room-temperature synthesis of lanthanide-doped $CaMoO_4$ nanocrystals. (b) Schematic of dual-ligand CaMoO4 nanocrystals. (c and d) Transmission electron microscopy (TEM) images of the as-synthesized $CaMoO_4$:15% Eu^{3+} nanocrystals. (e) Schematic illustrating the self-assembly process for fabricating a colloidal scintillator film. (f and g) Photographs of $CaMoO_4$:15%Eu^{3+} scintillator films produced through self-assembly of colloidal solutions using (f) cyclohexane and (g) *n*-hexanol as solvents. Scale bar = 1 cm. (h) UV-vis diffuse reflectance spectra of $CaMoO_4$ and $CaMoO_4$:15%Eu^{3+} nanocrystalline films. (i) X-ray diffraction (XRD) patterns of $CaMoO_4$:Ln^{3+} colloidal glasses. (j and k) Cross-sectional scanning electron microscopy (SEM) images of self-assembled $CaMoO_4$:15%Eu^{3+} film after solvent evaporation using (j) cyclohexane and (k) *n*-hexanol as solvents. Scale bar = 100 μm.

suitable as host materials for transparent ceramics and glass.[30,31] To elucidate the optical properties of the colloidal glass film, we obtained UV-vis diffuse reflectance spectra for $CaMoO_4$ and $CaMoO_4$:15%Eu^{3+} NC films (Fig. 1h). The undoped $CaMoO_4$ nanocrystals, synthesized *via* the same room-temperature co-precipitation method, formed a comparable transparent colloidal film through the self-assembly method. A strong absorption band in the 200–350 nm UV region can be attributed to the $CaMoO_4$ host lattice and $O^2 \rightarrow Mo^{6+}$ charge transfer transition.[32,33] The $CaMoO_4$:15% Eu^{3+}spectrum exhibited a blue-shifted absorption band due to Eu^{3+} ion doping, with multiple absorption bands corresponding to forbidden 4f–4f electronic transitions of Eu^{3+} ions: 362 nm ($^7F_0 \rightarrow {}^5D_4$), 382 nm ($^7F_0 \rightarrow {}^5L_7$), 395 nm ($^7F_0 \rightarrow {}^5L_6$), 416 nm ($^7F_0 \rightarrow {}^5D_3$), and 465 nm ($^7F_0 \rightarrow {}^5D_2$). X-ray diffraction (XRD) analysis of the transparent colloidal film confirmed the retention of the crystalline structure, with diffraction peaks closely matching the standard tetragonal scheelite $CaMoO_4$ reference pattern (Fig. 1i). The peak broadness indicates the film's polycrystalline nature.

Solvent selection critically determines nanoparticle superlattice quality and uniformity. During the evaporation-induced self-assembly process, capillary forces drive nanoparticles into dense, ordered configurations. However, the assembly mechanism depends on the delicate balance between interparticle forces and evaporation rate, which governs kinetic pathways. Nonpolar solvents (cyclohexane, petroleum ether) and weakly polar solvents (toluene) typically exhibit weak interactions with short-chain ligands, promoting particle clustering during drying. Their rapid evaporation rates facilitate aggregation, resulting in porous or irregular films. Conversely, moderately polar solvents (ethanol, *n*-hexanol, chloroform) better maintain nanocrystal stability and prevent aggregation. Moreover, moderate-volatility solvents like *n*-hexanol and chloroform enable slower evaporation, allowing nanoparticles to reorganize into highly ordered superlattices. While polar solvents such as water and ethanol can generate strong capillary forces to consolidate nanoparticles, their elevated surface tension may induce film shrinkage and cracking due to uneven stress distribution during evaporation. Their relatively slower evaporation rates facilitate gradual stress release, promoting uniform film formation. Through systematic solvent optimization, we identified *n*-hexanol as an optimal solvent, offering both moderate surface tension and volatility, achieving a balanced approach to

producing smooth, crack-free colloidal glass films. Consequently, transparent nanocrystalline films formed from nanocrystals dispersed in deionized water, ethanol, *n*-hexanol, and chloroform, with *n*-hexanol yielding particularly uniform and well-integrated transparent films. In contrast, nanocrystals dispersed in toluene, cyclohexane, and petroleum ether produced only white solids, failing to form transparent films (Fig. 2a).

To elucidate the self-assembly mechanism, we monitored particle suspensions at various evaporation stages (Fig. 2b), using the *n*-hexanol NC system as a model. During the initial evaporation phase, the $CaMoO_4$:15%Eu^{3+}NC colloidal solution gradually transformed into a white suspension. According to Rayleigh scattering theory, the light transmittance (T) of a particle-containing film can be described by the following formula:[34,35]

$$T = \exp\left\{\frac{-32\pi^4 d V_f r^3}{\lambda^4}\left(\frac{n_p}{n_m} - 1\right)\right\}$$

where d is the thickness of the composite film, V_f is the volumetric fraction of NPs, r is the radius of NPs, and n_p and n_m are the refractive indexes of NPs and matrix, respectively. Throughout the evaporation process, V_f gradually increases, potentially inducing nanoparticle agglomeration. Due to the difference between n_p and the residual solvent n_m, Rayleigh scattering occurs when light traverses the suspension. Larger nanoparticle agglomeration radii further compromise transparency, resulting in an opaque suspension. In the final solvent evaporation stage, as the solvent volume diminishes and V_f approaches 100%, colloidal particles densely pack, driven by solvent molecular traction and inter-particle attraction. Upon complete solvent evaporation, only tightly packed colloidal nanoparticles remain. Rayleigh scattering, caused by refractive index disparities between particles and solvent, progressively weakens and ultimately disappears. The densely assembled wide-bandgap nanocrystals effectively suppress visible light absorption and scattering, culminating in a uniform, transparent colloidal glass film.

To validate our hypotheses and investigate the internal structure of nanocrystalline solid films, we conducted scanning electron microscopy (SEM) analysis on cross-sections of transparent colloidal films formed by ethanol and hexanol

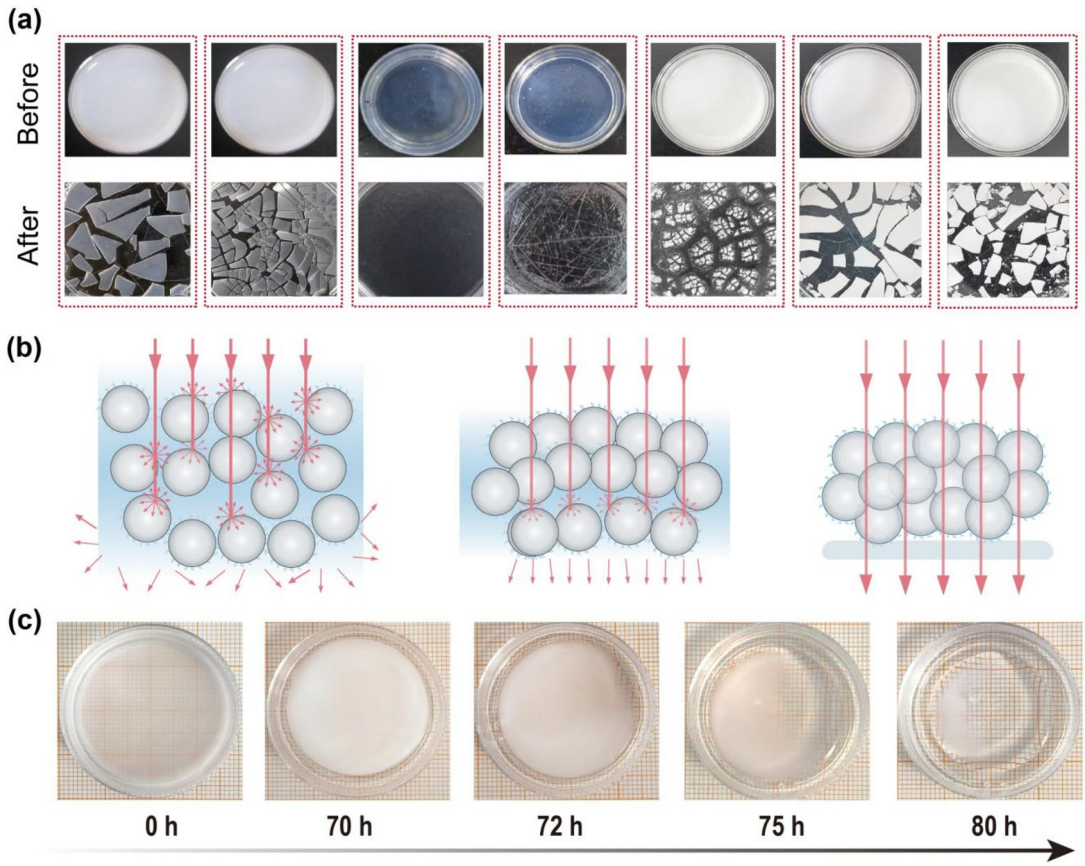

Fig. 2 Solvent-dependent self-assembly of $CaMoO_4$:15%Eu^{3+} nanocrystals. (a) Optical images of colloidal solids formed through solvent evaporation-induced self-assembly of $CaMoO_4$:15%Eu^{3+} nanocrystals dispersed in various solvents including deionized water, ethanol, *n*-hexanol, chloroform, toluene, cyclohexane and petroleum ether (from left to right). Inset shows photographs of $CaMoO_4$:15%Eu^{3+} nanocrystals dispersed in the corresponding solvents. (b) Schematic illustration demonstrating how $CaMoO_4$:15%Eu^{3+} nanocrystals form closely packed solids during solvent evaporation, resulting in reduced light scattering. (c) Photographs depicting the transformation process of $CaMoO_4$:15%Eu^{3+} suspension during *n*-hexanol solvent evaporation at room temperature.

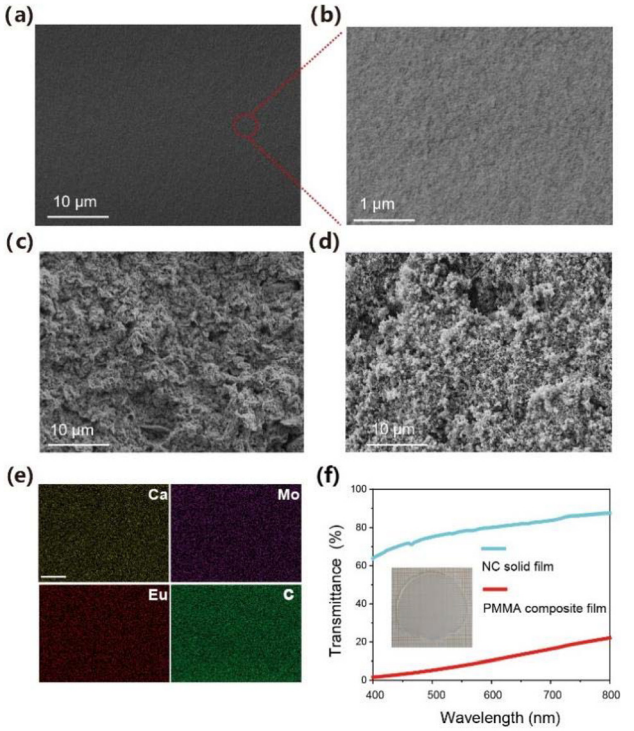

Fig. 3 (a–d) Cross-sectional SEM images of $CaMoO_4$:15%Eu^{3+} colloidal glass films obtained from nanocrystals dispersed in (a and b) *n*-hexanol, (c) cyclohexane and (d) petroleum ether. (e) Elemental mapping images for the cross-sectional view of $CaMoO_4$:15%Eu^{3+} films obtained after solvent evaporation using *n*-hexanol. Scale bar = 1 μm. (f) Transmittance spectra of 250 μm $CaMoO_4$:15%Eu^{3+} colloidal glass film and $CaMoO_4$:15%Eu^{3+} nanocrystal-doped PMMA composite film with 25 wt% nanocrystal loading. Inset shows the corresponding photograph of composite film.

solutions, and white solid films produced by cyclohexane and petroleum ether (Fig. 3c and d). Cross-sectional SEM images of the hexanol-derived colloidal glass film revealed a remarkably uniform and dense nanocrystal aggregation structure, devoid of observable cracks or pores (Fig. 3a and b). High-magnification energy-dispersive X-ray spectroscopy (EDS) mapping confirmed the homogeneous distribution of elements Ca, Mo, Eu, and C throughout the colloidal glass (Fig. 3e, Fig. S3†), with the carbon signal originating from the butyric acid and butylamine ligands capping the $CaMoO_4$:15%Eu^{3+} nanocrystal surfaces. Similarly, cross-section and magnified SEM images of ethanol-derived colloidal films demonstrated consistent uniformity and dense nanoparticle packing (Fig. S4†). These findings substantiate the self-assembly of $CaMoO_4$:15%Eu^{3+} nanocrystals into a densely packed structure during the final stages of polar solvent evaporation. In marked contrast, solid films obtained from cyclohexane and petroleum ether solutions exhibited significant irregular defects and porosity (Fig. 3c and d), underscoring the critical role of solvent polarity in the evaporation-induced self-assembly process and nanocrystal packing. Thermogravimetric analysis measurements of ethanol-derived and hexanol-derived colloidal glass were conducted (Fig. S5†). Considering the large specific surface area of $CaMoO_4$:15%Eu^{3+} nanocrystals, the mass loss of the samples during heating can be attributed to the removal of surface ligands from the particles. The residues after 600 °C account for 82.3 wt% and 81.2 wt%, respectively.

Moreover, a composite film of identical thickness was created by blending $CaMoO_4$:15%Eu^{3+} NCs with polymethyl methacrylate (PMMA) at a 1 : 3 mass ratio (Fig. 3f). The evaporation-induced self-assembly process resulted in a remarkable film with over 80% transmittance. In stark contrast, the PMMA composite film, prepared using conventional methods, exhibited significant transmittance deterioration due to the substantial refractive index mismatch between the crystal (n_{CaMoO_4} = 1.97)[36] and the polymer (n_{PMMA} = 1.49).

To demonstrate the versatility of the self-assembly method, we synthesized different lanthanide-doped nanocrystals with small sizes (~3 nm) for colloidal glass film preparation. $CaMoO_4$:10%Tb^{3+}, YVO_4, and $LaPO_4$ nanocrystals were synthesized at room temperature (Fig. S6–9†), yielding transparent colloidal films (Fig. S10 and 11†). The YVO_4 nanocrystal films exhibited relatively lower quality compared to $CaMoO_4$:10% Tb^{3+} and $LaPO_4$ counterparts (Fig. S12†).

The steady-state photoluminescence (PL) spectra of the colloidal films revealed characteristic red and green emissions from Eu^{3+} and Tb^{3+} ions, respectively, under ultraviolet light excitation (Fig. S13†). The emission peaks demonstrated a substantial Stokes shift relative to the excitation band, indicating negligible self-absorption—a property rendering these colloidal glass films exceptionally suitable for X-ray imaging applications. Time-resolved emission decay measurements were conducted for $CaMoO_4$:15%Eu^{3+} and $CaMoO_4$:10%Tb^{3+} colloidal glass films (Fig. S14†).

We anticipate that our transparent colloidal glass films will generate substantial light output when $CaMoO_4$:Ln^{3+} colloidal glasses are excited by X-rays. Generally, during scintillation in $CaMoO_4$:Ln^{3+} nanocrystals (Fig. 4a and Fig. S15†), X-ray photons interact with lattice heavy atoms, generating deep holes (h^+) in the core band and hot electrons (e^-) in the conduction band *via* photoelectric and Compton scattering. Secondary electrons from inelastic electron–electron scattering and Auger processes stimulate numerous electron–hole pair generations. These pairs subsequently diffuse to Eu^{3+} and Tb^{3+} luminescence centers, recombining to produce intense emissions.[37,38]

We compared the X-ray photon absorption coefficients of $CaMoO_4$:15%Eu^{3+} and the commercial scintillator bismuth germanate (BGO). Within the medical diagnostic energy range of 30–80 keV, the X-ray absorption efficiencies of both materials exhibit a notable similarity, revealing consistent radiative interaction characteristics (Fig. 4b). The consistent peak positions and intensities of radioluminescence (RL) and PL spectra confirm that luminescence originates from radiative recombination of excitons at lanthanide ion centres. The RL responses of $CaMoO_4$:15%Eu^{3+} and $CaMoO_4$:10%Tb^{3+} significantly surpassed that of the BGO scintillator (Fig. 4c). Sharp emission peaks at 614 nm ($^5D_0 \rightarrow {}^7F_2$ transition of Eu^{3+} ions) and 546 nm ($^5D_4 \rightarrow {}^7F_5$ transition of Tb^{3+} ions) demonstrated

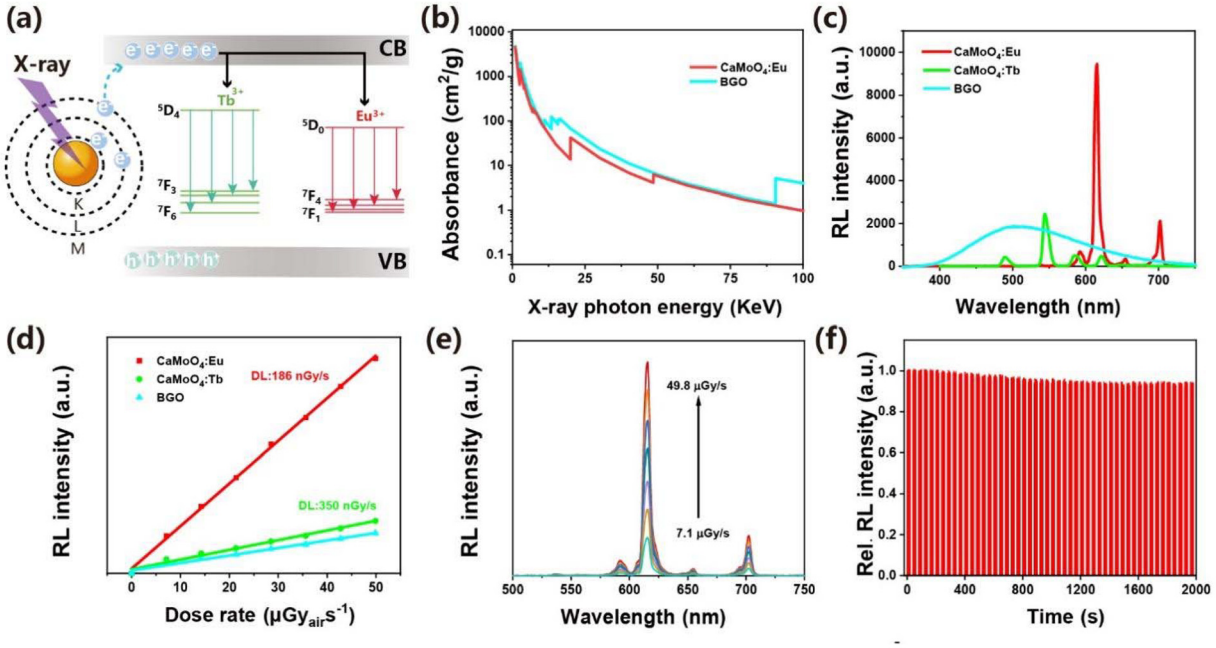

Fig. 4 Performance characterizations of $CaMoO_4:Ln^{3+}$ colloidal glass scintillators. (a) Schematic illustration of the radioluminescence mechanism in $CaMoO_4:Ln^{3+}$ scintillators. (b) X-ray absorption coefficients of $CaMoO_4$:15%Eu^{3+} compared to a commercial BGO scintillator. The attenuation coefficient was derived from the Photon Cross-Section Database. (c) Radioluminescence spectra of $CaMoO_4:Ln^{3+}$ colloidal glass and BGO scintillator under X-ray excitation. (d) Linear relationship between dose rate and signal intensities for $CaMoO_4:Ln^{3+}$ colloidal glass films and BGO scintillator. (e) Dosage-dependent radioluminescence spectra of the $CaMoO_4$:15%Eu^{3+} colloidal glass film over the dosage range of 7.1–49.8 μGy s^{-1}. (f) Radiation stability of $CaMoO_4$:15%Eu^{3+} colloidal glass scintillators under cyclic X-ray irradiation (dose rate: 550 μGy s^{-1}).

5.2- and 1.3-times higher RL emission intensities than the BGO scintillator, respectively.

RL intensities of the colloidal films demonstrated linear correlation with X-ray dose rates (Fig. 4d and e). The detection limit (DL), estimated at a signal-to-noise ratio of 3, was 186 nGy s^{-1}—approximately 30 times lower than standard medical diagnostic requirements (5.5 μGy s^{-1}). Under continuous X-ray irradiation for 30 minutes and repeated excitation across 50 cycles (20 s interval, 550 μGy s^{-1} dose rate), the $CaMoO_4$:15%Eu^{3+} RL intensity decreased by merely 6% from its initial value (Fig. 4f). Concurrently, $CaMoO_4$:10%Tb^{3+} exhibited negligible RL property alterations (Fig. S16†), demonstrating exceptional environmental stability and durability under prolonged X-ray exposure.

X-ray imaging performance was evaluated using a custom-built imaging system (Fig. 5a). Target objects were positioned before the scintillator films and exposed to an X-ray source to reveal internal structures. Spatial resolution was assessed *via* the modulation transfer function (MTF) using the slanted-edge method (Fig. 5b). At ultralow X-ray excitation conditions (20 kV, 30 μA), the spatial resolution—defined as the spatial frequency at MTF of 0.2—reached 27.1 lp mm^{-1}. This resolution substantially exceeds those of many previously reported transparent single crystals, polycrystalline films, and ceramic scintillators (Table S1†). Fig. 5c and d illustrate a steel spring concealed within a plastic capsule and a chip's internal structure—invisible to the naked eye but clearly discernible under X-ray irradiation due to differential X-ray attenuation.

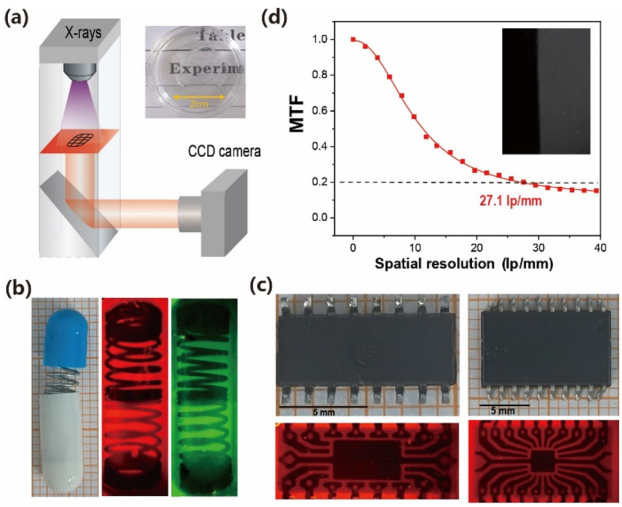

Fig. 5 X-ray imaging using colloidal glass scintillation films. (a) Schematic illustration of the X-ray imaging experimental setup: a colloidal glass film serves as the scintillator screen, with the sample positioned between the X-ray source and a digital camera. (b) Modulation Transfer Function (MTF) from a slanted-edge image, demonstrating a spatial resolution of 27.1-line pairs per millimeter (lp mm^{-1}). (c and d) Optical and X-ray image of (c) a steel wire inside a capsule. (d) Optical and X-ray image of electronic chips.

Conclusions

In conclusion, we innovatively integrated room-temperature coprecipitation with solvent evaporation self-assembly to develop $CaMoO_4$:Ln^{3+} colloidal glasses composed entirely of high-luminescence nanocrystals. By meticulously regulating and monitoring the self-assembly environment, we elucidated the formation mechanism of the dense, tightly packed transparent nanocrystalline film. The $CaMoO_4$:15%Eu^{3+} colloidal glass demonstrates exceptional optical and detection characteristics, exhibiting over 80% transmittance across the visible light spectrum and achieving a remarkable detection limit of 186 nGy s^{-1}. These properties translate to an impressive imaging resolution of 27.1 lp mm^{-1}. The exceptional performance of this self-assembled scintillator glass originates from its tightly packed, wide-bandgap nanocrystals, which effectively mitigate undesirable light absorption and scattering while maximizing nanoparticle concentration. The fully room-temperature manufacturing process and solution-processable nature of these scintillators represent a significant advancement over conventional scintillator materials, promising revolutionary potential in advanced X-ray imaging technologies.

Author contributions

Y. M. W. and J. X. conceived and designed the experiments. L. Z. synthesized the lanthanide nanomaterials. L. Z. and Y. W. W. conducted the optical experiments and characterization. L. Z. and X. Q. performed the X-ray imaging experiment. Y. M. W., J. X., Z. L., and S. L. wrote the paper with input from all authors.

Data availability

The data supporting this article have been included as part of the ESI.†

Conflicts of interest

There are no conflicts to declare.

Acknowledgements

Y. M. W. acknowledges the financial support from the National Natural Science Foundation of China (grant no. 52372156, 2024YFA1410900 and 62288102).

References

1 Q. Chen, J. Wu, X. Ou, B. Huang, J. Almutlaq, A. A. Zhumekenov, X. Guan, S. Han, L. Liang, Z. Yi, J. Li, X. Xie, Y. Wang, Y. Li, D. Fan, D. B. L. Teh, A. H. All, O. F. Mohammed, O. M. Bakr, T. Wu, M. Bettinelli, H. Yang, W. Huang and X. Liu, *Nature*, 2018, **561**, 88–93.
2 M. Nikl and A. Yoshikawa, *Adv. Opt. Mater.*, 2015, **3**, 463–481.
3 J. H. Heo, D. H. Shin, J. K. Park, D. H. Kim, S. J. Lee and S. H. Im, *Adv. Mater.*, 2018, **30**, 1801743.
4 C. Dujardin, E. Auffray, E. Bourret-Courchesne, P. Dorenbos, P. Lecoq, M. Nikl, A. N. Vasil'ev, A. Yoshikawa and R. Y. Zhu, *IEEE Trans. Nucl. Sci.*, 2018, **65**, 1977–1997.
5 L. Lu, M. Sun, T. Wu, Q. Lu, B. Chen and B. Huang, *Nanoscale Adv.*, 2022, **4**, 680–696.
6 R. Sun, Z. Wang, H. Wang, Z. Chen, Y. Yao, H. Zhang, Y. Gao, X. Hao, H. Liu and Y. Zhang, *ACS Appl. Mater. Interfaces*, 2022, **14**, 36801–36806.
7 W. Xiang, D. Shen, X. Zhang, X. Li, Y. Liu and Y. Zhang, *ACS Appl. Mater. Interfaces*, 2024, **16**, 4918–4924.
8 X. Zhang, Y. Shi, X. Wang, Y. Liu and Y. Zhang, *ACS Nano*, 2022, **16**, 21576–21582.
9 Z. Lin, S. Lv, Z. Yang, J. Qiu and S. Zhou, *Adv. Sci.*, 2022, **9**, 2102439.
10 X. Wang, X. Zhang, Y. Liu and Y. Zhang, *Chem. Eng. J.*, 2024, **483**, 149239.
11 S. P. Wang, O. Laudi, H. Lucks, K. A. Wickersheim and R. A. Buchanan, *IEEE Trans. Nucl. Sci.*, 1970, **17**, 49–56.
12 C. D. Brandle, *J. Cryst. Growth*, 2004, **264**, 593–604.
13 J. H. Xu, R. Luo, Z. Luo, J. Xu, Z. Mu, H. Bian, S. Y. Chan, B. Y. H. Tan, D. Chi, Z. An, G. Xing, X. Qin, G. C. Xing, Y. Wu and X. Liu, Ultrabright molecular scintillators enabled by lanthanide-assisted near-unity triplet exciton recycling, *Nat. Photonics*, 2025, **19**, 71–78.
14 A. Yoneyama, R. Baba and M. Kawamoto, *Opt. Mater. Express*, 2021, **11**, 398–411.
15 P. P. Fedorov, A. A. Luginina and A. I. Popov, *J. Fluor. Chem.*, 2015, **172**, 22–50.
16 Z. Li, C. Chen, W. Shen, D. Zhou, L. R. Jensen, X. Qiao, J. Ren, J. Du, Y. Zhang, J. Qiu and Y. Yue, *Adv. Opt. Mater.*, 2022, **10**, 2102713.
17 S. Lin, H. Lin, C. Ma, Y. Cheng, S. Ye, F. Lin, R. Li, J. Xu and Y. Wang, *Light: Sci. Appl.*, 2020, **9**, 22.
18 H. Y. Jeong, J. H. Lee, S. Y. Lee, J. Lee and S. O. Cho, *ACS Omega*, 2021, **6**, 33224–33230.
19 X. Ou, X. Qin, B. Huang, J. Zan, Q. Wu, Z. Hong, L. Xie, H. Bian, Z. Yi, X. Chen, Y. Wu, X. Song, J. Li, Q. Chen, H. Yang and X. Liu, *Nature*, 2021, **590**, 410–415.
20 L. Yang, Z. Li, L. He, J. Sun, J. Wang, Y. Wang, M. Li, Z. Zhu, X. Dai, S. X. Hu, F. Zhai, Q. Yang, Y. Tao, Z. Chai, S. Wang and Y. Wang, *Angew. Chem., Int. Ed.*, 2023, **62**, e202306465.
21 M. S. A. Hussien, M. I. Mohammed and I. S. Yahia, *Environ. Sci. Pollut. Res.*, 2020, **27**, 45225–45237.
22 J. Ma, W. Zhu, L. Lei, D. Deng, Y. Hua, Y. M. Yang, S. Xu and P. N. Prasad, *ACS Appl. Mater. Interfaces*, 2021, **13**, 44596–44603.
23 Y. Ling, X. Zhao, P. Hao, Y. Song, J. Liu, L. Zhao, Y. Qian and C. Guo, *Chem. Eng. J.*, 2023, **476**, 146790.

24 Y. Li, Y. Xu, Y. Yang, Z. Jia, H. Tang, J. B. Patel and Q. Lin, *Adv. Opt. Mater.*, 2023, **11**, 2300169.
25 Q. Cao, M. Liu, X. Shi, Z. Ni, B. Li, C. Lu and D. Pan, *Dalton Trans.*, 2023, **52**, 4663–4668.
26 M. Liu, X. Shi, Q. Cao, B. Li, Z. Ni, C. Lu, D. Pan and B. Zou, *Small*, 2023, **19**, 2301680.
27 H. Zargartalebi, S. H. Hejazi and A. Sanati-Nezhad, *Nat. Commun.*, 2022, **13**, 3085.
28 A.-Q. Xie, Q. Li, Y. Xi, L. Zhu and S. Chen, *Acc. Mater. Res.*, 2023, **4**, 403–415.
29 K. K. Price, Y. Wu, A. V. McCormick and L. F. Francis, *J. Am. Ceram. Soc.*, 2015, **98**, 2214–2222.
30 Z. Xiao, S. Yu, Y. Li, S. Ruan, L. B. Kong, Q. Huang, Z. Huang, K. Zhou, H. Su, Z. Yao, W. Que, Y. Liu, T. Zhang, J. Wang, P. Liu, D. Shen, M. Allix, J. Zhang and D. Tang, *Mater. Sci. Eng., R*, 2020, **139**, 100518.
31 J. Shi, J. Zhang, L. Yang, M. Qu, D.-C. Qi and K. H. L. Zhang, *Adv. Mater.*, 2021, **33**, 2006230.
32 V. M. Longo, L. S. Cavalcante, E. C. Paris, J. C. Sczancoski, P. S. Pizani, M. S. Li, J. Andrés, E. Longo and J. A. Varela, *J. Phys. Chem. C*, 2011, **115**, 5207–5219.
33 B. P. Singh, Maheshwary, P. V. Ramakrishna, S. Singh, V. K. Sonu, S. Singh, P. Singh, A. Bahadur, R. A. Singh and S. B. Rai, *RSC Adv.*, 2015, **5**, 55977–55985.
34 H. P. Dorum, E. Aksnes, S. Nilsson and P. G. Bjorholt, *Tidsskr. Nor. Laegeforen.*, 1980, **100**, 1–13.
35 H. Althues, J. Henle and S. Kaskel, *Chem. Soc. Rev.*, 2007, **36**, 1454–1465.
36 C. Bouzidi, K. Horchani-Naifer, Z. Khadraoui, H. Elhouichet and M. Ferid, *Phys. B*, 2016, **497**, 34–38.
37 B. Zheng, J. Fan, B. Chen, X. Qin, J. Wang, F. Wang, R. Deng and X. Liu, *Chem. Rev.*, 2022, **122**, 5519–5603.
38 J. Liu, X. Zhao, Y. Xu, H. Wu, X. Xu, P. Lu, X. Zhang, X. Zhao, M. Xia, J. Tang and G. Niu, *Laser Photonics Rev.*, 2023, **17**, 2300006.